

Light scattering by epitaxial VO₂ films near the metal-insulator transition point

Sergiy Lysenko,^{1,a)} Felix Fernández,¹ Armando Rúa,¹ Joaquin Aparicio,² Nelson Sepúlveda,³ Jose Figueroa,¹ Kevin Vargas,¹ and Joseph Cordero¹

¹Department of Physics, University of Puerto Rico, Mayaguez, Puerto Rico 00681, USA

²Department of Physics, University of Puerto Rico-Ponce, Ponce, Puerto Rico 00732, USA

³Department of Electrical and Computer Engineering, Michigan State University, East Lansing, Michigan 48824, USA

(Received 15 February 2015; accepted 1 May 2015; published online 14 May 2015)

Experimental observation of metal-insulator transition in epitaxial films of vanadium dioxide is reported. Hemispherical angle-resolved light scattering technique is applied for statistical analysis of the phase transition processes on mesoscale. It is shown that the thermal hysteresis strongly depends on spatial frequency of surface irregularities. The transformation of scattering indicatrix depends on sample morphology and is principally different for the thin films with higher internal elastic strain and for the thicker films where this strain is suppressed by introduction of misfit dislocations. The evolution of scattering indicatrix, fractal dimension, surface power spectral density, and surface autocorrelation function demonstrates distinctive behavior which elucidates the influence of structural defects and strain on thermal hysteresis, twinning of microcrystallites, and domain formation during the phase transition. © 2015 AIP Publishing LLC.

[<http://dx.doi.org/10.1063/1.4921057>]

INTRODUCTION

Metal-Insulator transition phenomenon in vanadium dioxide receives much attention since Morin's discovery.¹ VO₂ shows unique transformation of structural, electronic, and optical properties above room temperature, at $T_c \simeq 340$ K.¹⁻⁸ Upon heating, VO₂ undergoes a first-order insulator-to-metal phase transition (PT) with reversible change of monoclinic symmetry to tetragonal one. A number of studies were focused on size-dependent transition in isolated nanoparticles and film grains due to importance of fundamental processes involved in the PT dynamics and prospective technological use of VO₂-based materials.⁹⁻¹⁵ The observations of spatially resolved PT in VO₂ at the nanoscale level were recently reported in several papers, which demonstrate noticeable size-dependent transition dynamics in nanoparticles and nanocrystalline films.¹⁶⁻²¹

Despite significant effort in experimental and theoretical study of VO₂, the problem related to the PT mechanism in this material is still far from complete understanding owing to variety of discrepant experimental data. Slight variations in sample morphology and stoichiometry result in considerable change of elastic, electronic, and optical properties near the critical point. While studies of PT in single-crystal nanobeams, nanorods, and nanoplatelets usually provide most reproducible data, the information about PT dynamics in epitaxial and polycrystalline VO₂ films is quite fragmentary. At the same time, the understanding of structural dynamics in thin films is of special interest, since different films represent stochastic or highly ordered model systems with different morphology and concentration of structural defects. It was shown recently²²⁻²⁴ that the stress and strain in VO₂ film significantly depend on film thickness, grain size, and substrate.

The new information about multi-scale structural PT and domain formation can bring better understanding of different physical processes near the PT point of VO₂.

In this paper, we demonstrate the influence of internal strain and morphology of epitaxial VO₂ films on thermally induced domain formation and PT dynamics at different spatial scales. Angle-resolved measurements of elastic light scattering were performed to obtain the power spectral density (PSD), fractal dimension, and autocorrelation function (ACF) of the surface near T_c . It is shown that the size and shape of hysteresis loop depend on surface spatial frequency due to grain-size-dependent elastic strain and/or concentration of structural defects. The thermal evolution of scattering pattern and surface morphology of strained continuous film is found considerably different as compared to the film with overcritical thickness, where strain is relaxed via misfit dislocations (MDs). We find that the internal elastic strain in thin VO₂ film is the main origin which affects scattering indicatrix, producing twinning of microcrystallites and domain formation during PT.

EXPERIMENTAL

The pulsed laser deposition (PLD) technique was applied to fabricate a set of VO₂ films on single-crystal (012)Al₂O₃ (r-cut) and (001)Al₂O₃ (c-cut) sapphire substrates. The ablation of metallic vanadium target was performed by excimer laser (Lambda Physik Compex 110) with wavelength $\lambda = 248$ nm (KrF excimer), 10-ns pulse duration, and 4 J/cm² fluence, and a chamber atmosphere of O₂ and Ar at 30 mTorr pressure. Gases were injected into chamber through separated mass flow controllers with 20:5 (O₂:Ar, cm³/min:cm³/min) flow rate. The X-ray diffraction patterns of all VO₂ films evidenced single monoclinic M₁-phase at room temperature.

^{a)}Electronic mail: sergiy.lysenko@upr.edu

Several laser sources were employed to study the thermally induced PT in VO₂. A continuous wave 8 mW semiconductor laser with wavelength $\lambda = 1310$ nm was used in optical transmission measurements, and a 2 mW He-Ne laser with $\lambda = 632.8$ nm was used as a probe light source in the light scattering experiment. The sample temperature was controlled by a Peltier heater.

The observation of light scattering was conducted with a scatterometer described elsewhere.^{25,26} This apparatus provided measurements of bidirectional-scatter-distribution-function

$$BSDF(\theta, \varphi) = \left[\frac{dI_{scatt}(\theta, \varphi)}{d\Omega} \right] \frac{1}{I_0 \cos \theta}, \quad (1)$$

where θ and φ are the polar and azimuthal scattering angles, respectively. I_0 is the intensity of incident light, dI_{scatt} is the intensity of light scattered into solid angle $d\Omega$.

Angle-resolved elastic light scattering is a powerful technique for statistical analysis of surface irregularities of different sizes.^{27–33} While this technique does not provide real-space imaging of the surface roughness or VO₂ domains, it produces direct reciprocal-space imaging with robust statistical information about distribution of the inhomogeneities. Any type of structural ordering on the mesoscale, self-organization, twinning of microcrystals, and domain formation produces sharp diffraction peaks or symmetric features (e.g., lines, rings, squares, rhombs, hexagons, etc.) in the scattering indicatrix. Complex evolution of the structure on different scales can be easily identified and monitored by measuring the scattering signal at certain angles.

In this work, the measured BSDF data were used for calculation of two-dimensional (2D) power spectral density function of the surface as

$$PSD_s(\vec{f}) = BSDF(\vec{f})/OF, \quad (2)$$

where OF is an optical factor which depends on dielectric permittivity and scattering angle.³³ OF was calculated using equations obtained by Elson in Ref. 34. The optical constants for these calculations were obtained from additional angular measurements of reflection coefficient and data fit for s- and p-polarization of incident light. The $PSD_s(f)$ function represents the statistical distribution of surface roughness versus surface spatial frequency $f = \sin \theta / \lambda$ and is the Fourier transform of the surface autocorrelation function $ACF(r)$.

The autocorrelation function defines correlation of surface irregularities versus the translation length r in the surface plane.³³ At zero translation $ACF(0) = \delta^2$, where δ is rms roughness. In this work, we use the normalized autocorrelation functions ACF/δ^2 , calculated from scattering (ACF_s) and atomic-force-microscopy data (ACF_{AFM}), where $ACF_s(0) = 1$ and $ACF_{AFM}(0) = 1$.

There are several instrumentation-dependent limitations to observe the structural dynamics by elastic light scattering such as wavelength and light polarization, angle of incidence, aberration of the optical system, and resolution of the charge-coupled device (CCD). The light scattering experiment depends on a significant number of different

parameters, and some of them can be unknown. The range of spatial frequencies available for observation is limited by the probe wavelength. In this work, the measurements were performed at normal incidence. The light scattered at $\theta = 90^\circ$ corresponds to the maximal spatial frequency available for observation, $f_{max} = \sin 90^\circ / \lambda = 1/\lambda$. The central part of the scattering indicatrix is blocked by the sample holder, which prevents measurement of the signal for low spatial frequencies $\leq 0.4 \mu\text{m}^{-1}$.

The Raman effect was measured in backscattering configuration from room temperature to 400 K by a Renishaw Raman Microspectrometer RM2000 system. The instrument was equipped with a CCD detector, Leica microscope, and a diode laser with wavelength $\lambda = 532$ nm.

The VO₂ film surface was also scanned by atomic-force-microscope (AFM, Park Scientific Instruments, Autoprobe CP). The AFM topography analysis, calculation of spectral density, and autocorrelation function of the surface roughness were performed with WSxM software.³⁵

RESULTS AND DISCUSSION

Surface morphology and domain formation

The distribution and orientation of crystalline domains in thin ferroelastic VO₂ film strongly depend on the strain field and correspond to the minimum of elastic energy. Self-organization of VO₂ domains is a complex problem related to the misfit strain ϵ_m between film and substrate, defects, and interference of strain fields from different crystallites. The influence of the substrate on the net strain is crucial. Thus, the parallel ordering of ferroelastic microcrystals in most cases reduces the long-order strain field,³⁶ as observed for nanoplatelets,^{16,21,37,38} nanobeams,³⁹ and for epitaxial VO₂ films on TiO₂⁴⁰ and Al₂O₃ single-crystal substrates.^{24,41–45} The r-cut sapphire substrate Al₂O₃ is characterized by a rectangular atomic lattice on the surface, and the VO₂ PLD film is strongly oriented on this substrate with directions $[010]_{VO_2} \parallel [100]_{Al_2O_3}$ and $[001]_{VO_2} \parallel [02\bar{1}]_{Al_2O_3}$. Some of these directions can be slightly misoriented within less than 1° .²⁵ Such a small misorientation is likely due to elastic interaction between different crystallites, defects and substrate.

The BSDF indicatrices of hemispherical light scattering are shown in Fig. 1(a) for 30-nm-thick VO₂/Al₂O₃(r-cut) film as a function of both polar θ and azimuthal φ angles. A distinctive feature of these indicatrices is a square-like pattern outlined by isophotes in the central area within $0^\circ < \theta \leq 55^\circ$. The isophotes are parallel to $[010]$ (b_m) and $[001]$ (c_m) directions of the epitaxial VO₂ film. At larger polar angles, this pattern loses its sharpness. A slight elongation of isophotes along $\varphi = 90^\circ, 270^\circ$ direction is due to intrinsic polarization anisotropy of the scattering process, since the polarization of incident light was oriented along this azimuthal direction. The power spectral density function PSD_s of the surface calculated from scattering indicatrix eliminates such polarization anisotropy [Fig. 1(b)]. Nevertheless, the square-like pattern remains in the center of the PSD_s map and is a signature of highly ordered domains in the film.

The texture of epitaxial films is highly influenced by the substrate and film thickness. In order to demonstrate this

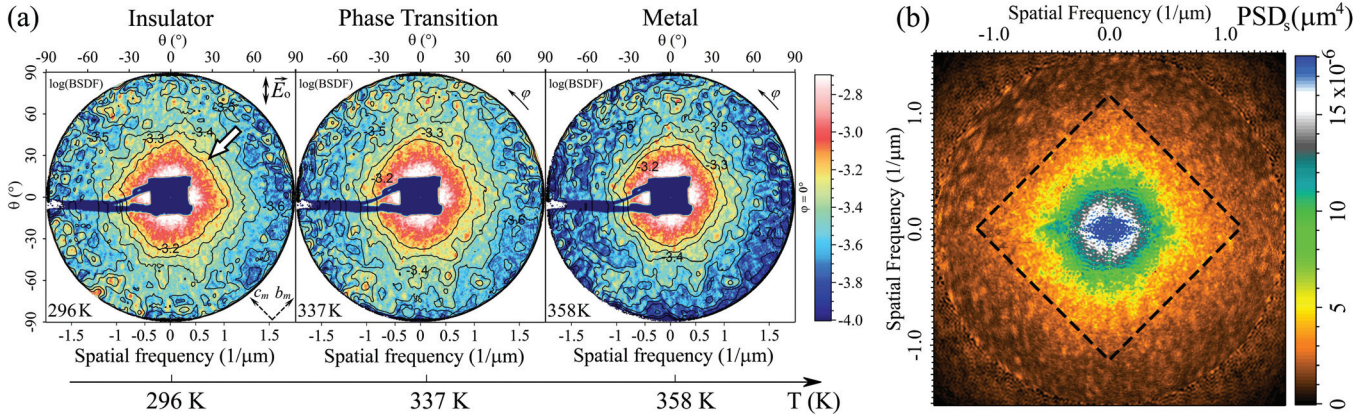


FIG. 1. (a) Temperature-dependent evolution of light scattering indicatrix for 30-nm-thick film $\text{VO}_2/\text{Al}_2\text{O}_3(\text{r-cut})$. Arrow marks a square-like pattern at $T = 296 \text{ K}$. (b) Power spectral density of the surface at $T = 296 \text{ K}$. Central and periphery region of PSD map was reconstructed using the Gerchberg-Saxton ER algorithm. Dashed isophotes outline the square-like pattern. (Multimedia view) [URL: <http://dx.doi.org/10.1063/1.4921057.1>]

influence, we show several scattering indicatrices obtained for VO_2 films deposited on c-cut Al_2O_3 (Fig. 2), which are considerably different as compared to indicatrices for $\text{VO}_2/\text{Al}_2\text{O}_3(\text{r-cut})$. In a series of previous XRD studies,^{24,42-44,46} it has been shown that the $\text{VO}_2/\text{Al}_2\text{O}_3(\text{c-cut})$ film undergoes 3-fold twinning. These films are highly textured with orientation of $[100]_{\text{VO}_2}$ domain axis along three equivalent crystallographic directions of $\text{Al}_2\text{O}_3(\text{c-cut})$ substrate. As a result, for uniformly twinned 50-nm-thick $\text{VO}_2/\text{Al}_2\text{O}_3(\text{c-cut})$ film the indicatrices show symmetric directions of scattering with 60° angular separation [Fig. 2(a)]. The local twinning of some films can produce more complex texture with rotation of domains by the angles other than 60° .^{42,47} Thus, the indicatrices for 30-nm-thick $\text{VO}_2/\text{Al}_2\text{O}_3(\text{c-cut})$ show the preferential directions of scattering with 45° and 75° angular separation [Fig. 2(b)]. This indicates the presence of domains

rotated by 45° and 75° . The specific domain formation in $\text{VO}_2/\text{Al}_2\text{O}_3(\text{c-cut})$ makes these films optically isotropic, while the films deposited on $\text{Al}_2\text{O}_3(\text{r-cut})$ retain their optical properties inherent to VO_2 single crystal.⁴² The local morphology of $\text{VO}_2/\text{Al}_2\text{O}_3(\text{r-cut})$ was found to be more uniform within the sample, as compared to $\text{VO}_2/\text{Al}_2\text{O}_3(\text{c-cut})$, and further discussion will be focused on optical properties of $\text{VO}_2/\text{Al}_2\text{O}_3(\text{r-cut})$.

The AFM data for 30-nm-thick $\text{VO}_2/\text{Al}_2\text{O}_3(\text{r-cut})$ films yield the rms roughness of the surface as $\delta = 96 \text{ \AA}$. Fig. 3(a)

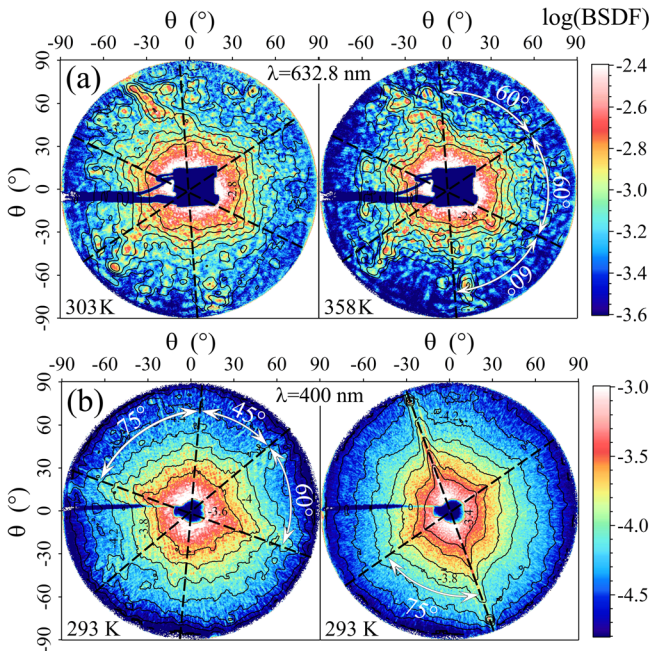


FIG. 2. The light scattering from $\text{VO}_2/\text{Al}_2\text{O}_3(\text{c-cut})$ films. (a) $\log(\text{BSDF})$ for 50-nm-thick film in insulating ($T = 303 \text{ K}$) and metallic ($T = 358 \text{ K}$) state. (b) $\log(\text{BSDF})$ for different areas of 30-nm-thick film obtained with $\lambda = 400 \text{ nm}$ laser wavelength. Dashed lines indicate preferential directions of scattering.

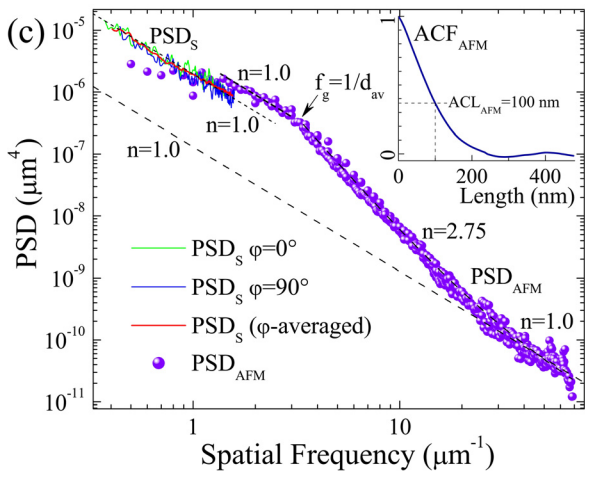
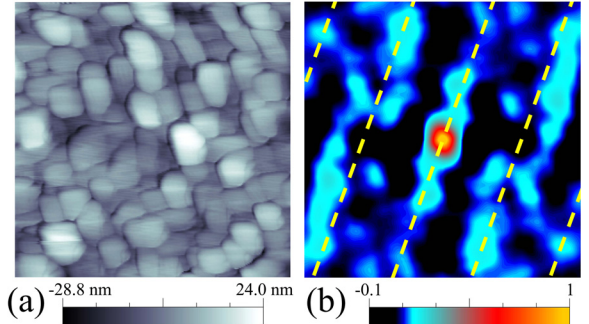


FIG. 3. Morphology of 30-nm-thick film $\text{VO}_2/\text{Al}_2\text{O}_3(\text{r-cut})$. (a) $2 \times 2 \mu\text{m}^2$ AFM topography and (b) $2 \times 2 \mu\text{m}^2$ surface autocorrelation function ACF_{AFM} . Periodical fringes are marked by dashed lines. (c) Power spectrum extracted from AFM and light scattering data at $T = 296 \text{ K}$. Dashed lines are fit by Eq. (3). The inset shows a cross-section of $2\text{D } \text{ACF}_{\text{AFM}}$.

shows that the lateral shape of VO₂ grains is somewhat rectangular, similar to nanorods studied by Sohn *et al.*⁴⁸ and Kim *et al.*⁴⁹ The average lateral size of VO₂ grains is $d_{av} \simeq 305$ nm, which corresponds to spatial frequency $f_g = 1/d_{av} = 3.3 \mu\text{m}^{-1}$. This range is unattainable in the scattering measurements since the maximal spatial frequency probed by the He-Ne laser is $f_{max} = 1/\lambda = 1.58 \mu\text{m}^{-1}$. However, the square-like pattern in the scattering indicatrix at $\theta < 55^\circ$ ($f < 1.3 \mu\text{m}^{-1}$) indicates that the VO₂ crystallites are organized into highly ordered clusters. Above $\theta = 55^\circ$, this pattern is distorted and less pronounced owing to increased randomness in orientation of smaller surface irregularities.

The 2D autocorrelation function of surface roughness calculated from AFM topography [Fig. 3(b)] shows a presence of isotropic and weak anisotropic components. The isotropic component of surface roughness contributes only in the central maximum of ACF_{AFM} with near-exponential decay within ~ 300 nm [inset in Fig. 3(c)] and, therefore, can be easily separated from the rest of ACF_{AFM} . A periodical anisotropic component results in the oscillation of ACF_{AFM} , showing fringes with period of $0.55 \mu\text{m}$. This indicates an ordering of microstructure along the fringe direction.

Taking into account AFM data, the observed indicatrices in Fig. 1 can be characterized in terms of fractal surface scattering where the scattered field contains information about sub-wavelength VO₂ crystallites organized in highly ordered square-like structures due to anisotropic ordering on the single-crystal r-cut sapphire substrate. The structure of epitaxial VO₂/Al₂O₃ films is a classic example of a “supercrystal,” where the groups of nanocrystals are organized in polysynthetic domains.³⁶ In contrast to a single-crystal, the “supercrystal” film is a quite flexible structure with relatively high mechanical mobility of nanocrystals. Thus, a small change in the elastic energy results in splitting of the film into domains of the same or different phases in order to reduce the net elastic energy.^{36,50} This is an intrinsic property of thin VO₂ films which qualitatively changes the temperature-dependent scattering pattern in Fig. 1(a).

The information about fractal properties of the sample was obtained from the power spectra PSD_{AFM} and PSD_s calculated from AFM topography and scattering data, respectively. It is noted that the data obtained from AFM and from elastic light scattering cover different ranges of spatial frequencies. Moreover, these experimental techniques are based on different physical processes of interaction between the probe (i.e., light or AFM tip) and the surface. The comparison of PSD_s and PSD_{AFM} functions shows their overlap [Fig. 3(c)]. Also, the slope of PSD_{AFM} within $f = 1.4\text{--}3.0 \mu\text{m}^{-1}$ coincides with the slope of PSD_s function. This indicates that the AFM and light scattering measurements yield the same information about fractal dimension of the surface. At lower spatial frequencies $f < 1.3 \mu\text{m}^{-1}$, the PSD_{AFM} function has only few data points, and within this range the accuracy of AFM measurement is slightly lower as compared to higher frequencies. Since the AFM is a conventional and precise tool to characterize surface roughness, the overlap between PSD_s and PSD_{AFM} data denotes a high precision of scattering measurements.

Both PSD functions show fractal-like behavior and can be characterized by 2D power spectrum⁵¹

$$\text{PSD}(f) = \frac{\Gamma[(n+1)/2]}{2\Gamma(1/2)\Gamma(n/2)} \cdot \frac{K_n}{f^{n+1}}, \quad (3)$$

where the K_n and n are constants. The Hausdorff-Besicovitch dimension is defined as $D = (5-n)/2$ and, along with K_n and n , is the fractal parameter of surface inhomogeneity.^{51–53}

The PSD_s functions at different azimuthal angles φ show the same slope in a log–log graph [Fig. 3(c)], indicating a relatively high isotropic component of surface roughness. Applying the fractal approach for analysis of surface roughness, one can expect the independence of the fractal parameters on experimental bandwidth. However, the fitting of PSD data with Eq. (3) shows some difference. The parameters obtained for PSD_s are $n=1$ ($D=2$), while the PSD_{AFM} shows multifractal behavior and can be described by a sum of PSD functions with $n=2.75$ ($D=1.13$) at $f=3.3\text{--}30 \mu\text{m}^{-1}$ and $n=1$ ($D=2$) at $f>30 \mu\text{m}^{-1}$ and $f=1.4\text{--}3.0 \mu\text{m}^{-1}$. It is important to note that the lower limit of the linear part of PSD_{AFM} with $n=2.75$ coincides with the spatial frequency of VO₂ crystallites $f_g = 3.3 \mu\text{m}^{-1}$. Moreover, the fractal parameters of PSD_s coincide with those of PSD_{AFM} at $f>30 \mu\text{m}^{-1}$ and $f=1.4\text{--}3.0 \mu\text{m}^{-1}$.

The PSD data in Fig. 3(c) reveal the multifractal structure of the film. The distribution of small VO₂ irregularities with $f>30 \mu\text{m}^{-1}$ likely replicates the Al₂O₃ substrate roughness. The obtained fractal dimension $D=2$ ($n=1$) corresponds to the *extreme fractal* and indicates close-packed crystallites of rugged surface.^{52,53} The distribution of larger VO₂ grains with $f_g < f < 30 \mu\text{m}^{-1}$ is organized into another fractal structure with $D=1.13$ ($n=2.75$) related to smoother surface. However at $f < f_g$ the VO₂ irregularities again are organized in domains with $D=2$ ($n=1$), as at $f>30 \mu\text{m}^{-1}$.

The averaged power spectra PSD_s calculated for 30-nm-thick film in insulating and metallic state show a noticeable difference in slope (see inset in Fig. 4(a)). The fractal dimension decreases from $D=2$ ($n=1$) to $D=1.85$ ($n=1.3$) during the PT, indicating a smoothing of surface irregularities in the metallic phase.

In terms of Rayleigh smooth-surface criterion,³³ the epitaxial VO₂ film with $\delta < \lambda/(4\pi)$ can be considered as optically smooth. For such surface the BSDF(f) is nearly scaled PSD function, as depicted in Fig. 4(a) for the cross-section of the scattering indicatrix at $\varphi = 0^\circ$, $T = 296$ K. Therefore, correct information about statistical distribution of surface inhomogeneities can be obtained directly from BSDF data. This is “scatter prediction” method that allows reconstructing the evolution of surface irregularities when the system is in nonequilibrium or quasi-equilibrium state, and material optical constants are unknown.

The distinctive feature of BSDF(θ), BSDF(f), and $\text{PSD}_s(f)$ for VO₂/Al₂O₃ is a presence of sharp peaks, as identified in Figs. 1 and 4. This is the typical signature of strong ordering of crystallites along different directions. The self-organized surface structures scatter light as differently oriented diffraction gratings whose period depends on film temperature. Thus, the BSDF undergoes noticeable change

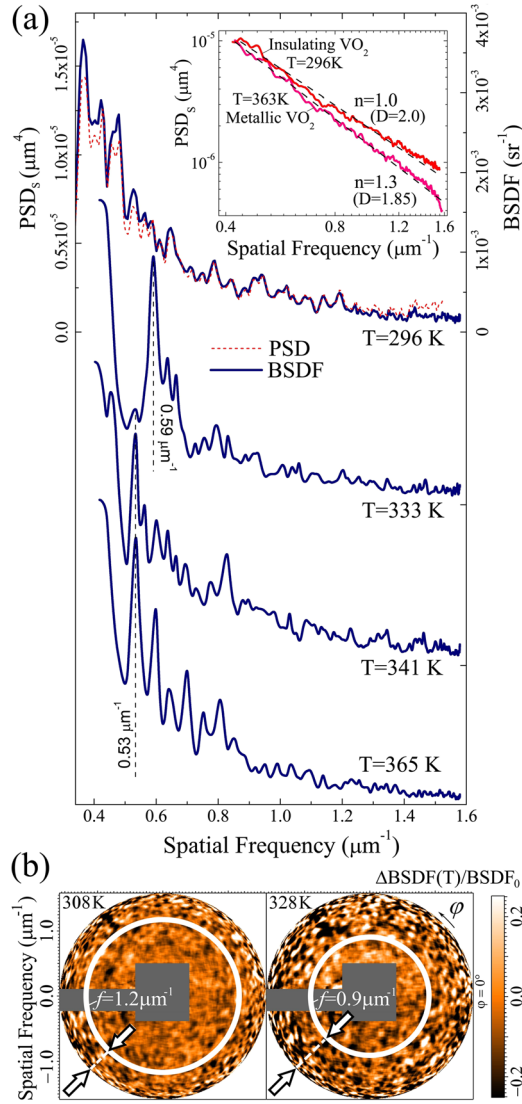


FIG. 4. The evolution of scattering pattern and power spectral density of the surface roughness for 30-nm-thick film $\text{VO}_2/\text{Al}_2\text{O}_3(\text{r-cut})$. (a) Cross-sections of the BSCDF scattering indicatrix and PSD_s at $\varphi = 0^\circ$. Inset shows the azimuthally averaged PSD_s function for insulating and metallic phases. Dashed lines are fit by Eq. (3). (b) The relative change $\Delta\text{BSCDF}(T)/\text{BSCDF}_0$ near the PT point, where BSCDF_0 is obtained for insulating VO_2 at $T = 296$ K, and $\Delta\text{BSCDF}(T) = \text{BSCDF}(T) - \text{BSCDF}_0$. Arrows mark the region that corresponds to the noticeable emergence of new diffraction peaks.

with temperature (Figs. 1 and 4). During the PT most diffraction peaks are shifting, emerging, or decaying due to twinning of VO_2 microcrystallites accompanied by “dynamic” domain formation process. Moreover, the evolution of scattering pattern begins well below the critical temperature T_c and persists well above it.

The emergence of new diffraction peaks can be observed in Fig. 4(b) at higher spatial frequencies above $f = 1.2 \mu\text{m}^{-1}$ already at $T = 308$ K. This figure indicates an isotropic formation of domains with sizes less than $d = 1/f = 0.83 \mu\text{m}$. As the temperature reaches $T = 328$ K, the region affected by the PT uniformly spreads to $f = 0.9 \mu\text{m}^{-1}$ ($d = 1/f = 1.1 \mu\text{m}$). With further temperature increase, new diffraction peaks uniformly fill up all scattering indicatrix. This temperature-dependent process corresponds to the realignment of domains and significantly varies from sample

to sample. The self-organized surface structure consists of parallel-sided VO_2 domains with period $d_D = \sqrt{2\gamma H/e_S}$, where γ is the specific surface energy of the domain boundary, H is the film thickness, and e_S is the specific surface energy of local deformations at the boundary between film and substrate.^{36,54} The spatial frequency of this structure is

$$f_D = \sqrt{\frac{e_S}{2\gamma H}} \quad (4)$$

Since $f_D \sim \sqrt{e_S/\gamma}$, a small change in the internal strain of the film or nucleation of new phase both result in the formation of new domain pattern, affecting the scattering indicatrix.

For 30-nm-thick $\text{VO}_2/\text{Al}_2\text{O}_3(\text{r-cut})$, the change in scattering indicatrix starts at room temperature, immediately when heating is applied. The arbitrary cross-section of the indicatrix at $T = 333$ K shows sharp peaks at $f \sim 0.6 \mu\text{m}^{-1}$ [$f = 0.59 \mu\text{m}^{-1}$ in Fig. 4(a)] which are assigned to strong ordering of VO_2 domains with a period of $d = 1.7 \mu\text{m}$. At the PT temperature $T_c = 341$ K, the structural inhomogeneity of the film becomes highest due to coexistence of different phases. The sharpness of the square-like pattern in the center of scattering indicatrix in Fig. 1 decreases. When the temperature reaches $T = 365$ K, the VO_2 has completely switched into its metallic R-phase and the new set of quasi-periodic diffraction peaks appears [starting at $f = 0.53 \mu\text{m}^{-1}$ in Fig. 4(a)]. This behavior corresponds to self-organization of domains in new periodic structures with minimal elastic energy.

Additional information about evolution of VO_2 structure was obtained from the autocorrelation function ACF_s calculated by Fourier transform of $\text{PSD}_s(f)$ and $\text{BSCDF}(f)$ using the Gerchberg-Saxton error reduction (ER) algorithm which significantly reduces numerical error.^{26,55,56} This algorithm was also applied to restore absent $\text{PSD}_s(f)$ data at the periphery up to $f = 2.1 \mu\text{m}^{-1}$ and in the central area of the scattering indicatrix blocked by the sample holder [Fig. 1(b)]. At some temperatures, the calculation of PSD_s was not performed, because of lack of information about VO_2 optical constants near the PT point. Therefore, ACF_s were calculated from BSCDF data instead of PSD_s , since $\text{BSCDF}(f)$ is practically a scaled $\text{PSD}_s(f)$ for a smooth surface, as discussed above and shown in Fig. 4(a).

Fig. 5(a) shows the ACF_s distribution for insulating and metallic phases versus translation length. The distinctive feature of ACF_s is a presence of *spatial oscillations* with ordered maxima due to domain formation in the epitaxial film. In insulating phase the noddied-type maxima are aligned in a mesh marked by dashed lines in Fig. 5(a), separated by $2.2 \mu\text{m}$. This structure of ACF_s is very similar to fringes of ACF_{AFM} separated by $0.55 \mu\text{m}$ [Fig. 3(b)]. It is very likely that the ACF_s represents the same highly ordered domains as ACF_{AFM} but with filtered out higher spatial harmonics, since the experimental bandwidths of AFM and light scattering experiments are substantially different.

The measure of surface inhomogeneity can be referenced to the autocorrelation length (ACL) of the surface. ACL is defined as the ACF halfwidth at the $\text{ACF}(0)/e$ point,

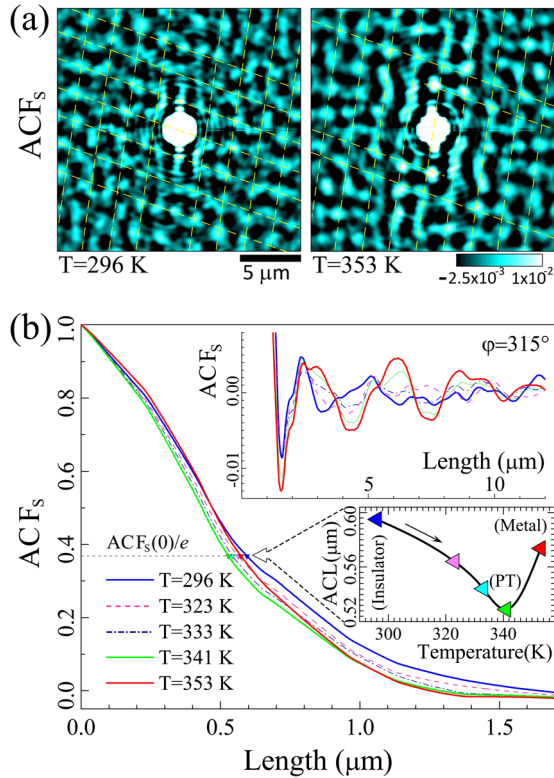


FIG. 5. (a) Autocorrelation function of VO_2 surface for insulating M_1 -phase ($T=296$ K) and metallic R -phase ($T=353$ K). (b) Cross-section of ACF_s distribution at different temperatures. Upper inset shows oscillatory component of ACF_s . Lower inset shows evolution of autocorrelation length versus temperature. (Multimedia view) [URL: <http://dx.doi.org/10.1063/1.4921057.2>]

and related to the uniform isotropic component of roughness and calculated from the central peak of ACF map. The difference in experimental bandwidth results in different values of ACL obtained by different techniques. Thus, the autocorrelation length $ACL_{AFM} = 100$ nm [inset in Fig. 3(c)] derived from AFM measurements is almost five times less than $ACL_s = 595$ nm calculated from scattering data at $T=296$ K [see inset in Fig. 5(b)]. As the temperature increases, the ACL_s decreases and reaches a 529 nm minimum at PT critical point $T_c = 341$ K. This indicates a gradual increase of disorder in the VO_2 film. However, after the PT at $T=353$ K, the order significantly increases and the ACL_s recovers to 574 nm. The noded maxima of ACF_s [Fig. 5(a)] migrate during the heating process and in the metallic phase they become more pronounced [see inset in Fig. 5(b)]. Their locations at $T=353$ K are not strictly aligned in a mesh as at $T=296$ K, and in vertical direction [Fig. 5(a)] the average separation between maxima at $T=353$ K shrinks to $1.8 \mu\text{m}$, indicating noticeable surface reconstruction.

There are two origins for surface scattering: inhomogeneity of the dielectric permittivity ϵ and geometrical roughness. Since below the PT point there are no metallic nuclei which could provide significant disorder in dielectric constant, it is difficult to assign the observed significant change of ACF_s , BPDF, and shift of diffraction peaks in Figs. 1(a) and 4 to scattering from temperature-dependent inhomogeneity of ϵ . The Raman scattering experiment conducted by

Atkin *et al.*⁵⁷ has shown that the intermediate M_2 -phase can nucleate in strained VO_2 at temperatures below T_c . However, nucleation of M_2 -phase during the heating process would not add noticeable disorder in ϵ either, since the dielectric constants of M_1 and M_2 phases are almost indistinguishable within the optical region. On the other hand, new M_2 -phase at the nanoscale can certainly change the strain field of polydomain VO_2 film and, as a result, can introduce further domain formation and new elastic deformations.

In this work, Raman scattering was measured at different temperatures of the film in order to verify the presence of M_2 -phase. Fig. 6 shows Raman spectra of stoichiometric VO_2 at different temperatures. As shown in Refs. 57–59, the distinctive signature of M_2 and T -phase in strained sample is splitting and blueshifting of the $A_g 613 \text{ cm}^{-1}$ phonon mode as well as decay of the low-frequency mode $A_g 194 \text{ cm}^{-1}$. Nevertheless, the Raman spectra in Fig. 6 do not show such behavior, indicating absence or low concentration of M_2 -phase at room temperature and near the PT point T_c . While even a small concentration of M_2 -phase can affect the net strain field, another origin of elastic strain in the film is a difference in thermal expansion of VO_2 ($5.78 \times 10^{-6} \text{ K}^{-1}$ at 298–334 K and $13.35 \times 10^{-6} \text{ K}^{-1}$ at 339–360 K)⁶⁰ and Al_2O_3 substrate ($8 \times 10^{-6} \text{ K}^{-1}$).⁶¹ This can produce a noticeable change in the strain field of the epitaxial film when the temperature changes by several degrees.

Taking into account Eq. (4) along with Raman scattering and thermal expansion data, the observed continuous evolution of BPDF within broad temperatures outside the PT range (Figs. 1 and 4) is assigned to domain formation and elastic deformation of the film due to strain effects. It is very likely that in the 30-nm-thick $\text{VO}_2/\text{Al}_2\text{O}_3$ the elastic strain, particularly misfit strain, is not relaxed via formation of static dislocation network. Instead, the strain relaxation is accompanied by “dynamic” temperature-dependent formation of twins, presumably oriented at $\sim 45^\circ$ angle to the substrate as observed by Zhao *et al.*⁴³ for $\text{VO}_2/\text{Al}_2\text{O}_3$ (*r*-cut) epitaxial film.

The conclusion about the presence of significant internal strain in thin VO_2 film is in agreement with data obtained in Ref. 22, where the absolute value of residual stress was found to be higher for thinner films. It was shown that the residual stress for the 100-nm-thick VO_2 film deposited on Si substrate by radio frequency (RF) sputtering is -677 MPa,

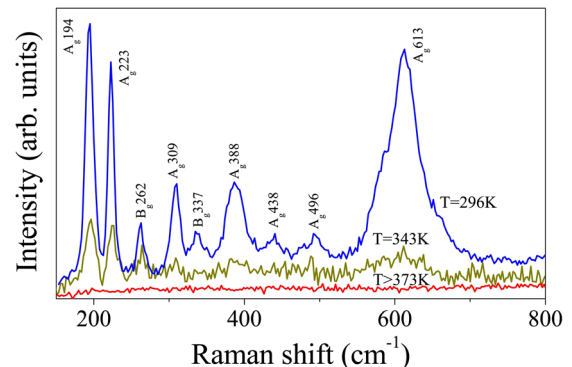


FIG. 6. Raman spectra of VO_2 at different temperatures.

and it changes to -73 MPa as the thickness increases to 440 nm. Moreover, the PT produces additional alteration of the stress. For PLD films grown on single-crystal Al_2O_3 (r-cut) substrate the absolute value of internal stress is certainly different and is expected to be higher due to epitaxial nature of the film.

The structure of epitaxial film remains continuous on the microscopic level upon full cycle of the PT process due to phase coherency. This coherency is attained by relaxation of structural strain via microdeformations at the grain boundaries and at the boundary which separates different VO_2 phases and domains. The strain energy is transferred into energy of structural microdeformations and/or defects.⁶² Suppressing the long-order macroscopic strain field in the epitaxial film, the microdeformations are non-coherent with the net strain field and are a residual origin of the strain. Therefore, the strain-assisted domain formation in the film starts mostly within the microdeformations. That is, at the boundary of neighboring grains or phases and at structural defects.

The angle-resolved light scattering technique provides direct statistical imaging of multi-scale grain-size-dependent transitions in the film. The thermal hysteresis of scattering signal for structures with different spatial frequencies f is shown in Fig. 7. We note that the smaller structures with higher spatial frequencies scatter light less and their contribution is almost hidden in the total scattering signal I_{scatt}/I_0 integrated within hemisphere. Therefore Fig. 7(a) shows normalized graphs of scattering signal I_{scatt}^* for different f , where

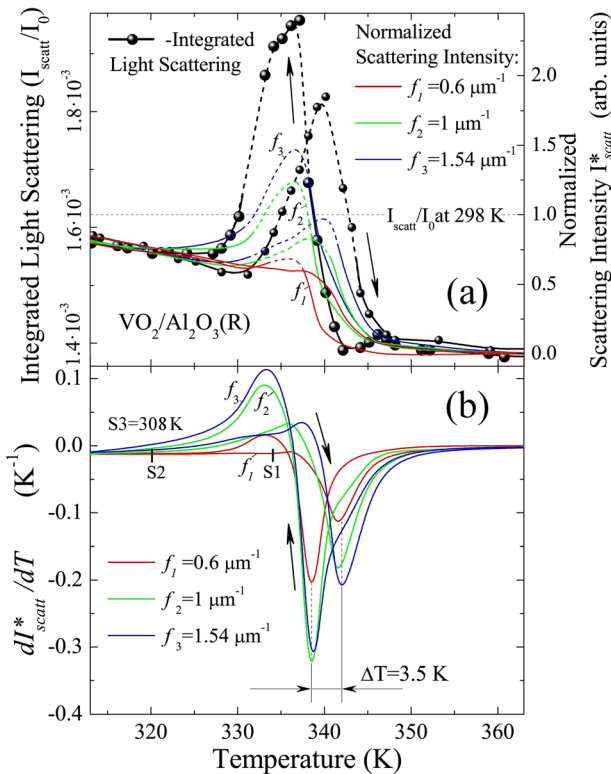


FIG. 7. (a) Hysteretic evolution of VO_2 scattering signal for integrated light scattering and for scattering by different spatial frequencies of the surface. (b) Derivative of normalized scattering intensity. Starting points of the PT for spatial frequencies $f_1 = 0.6 \mu\text{m}^{-1}$, $f_2 = 1 \mu\text{m}^{-1}$, and $f_3 = 1.54 \mu\text{m}^{-1}$ are marked as S1, S2, and S3, correspondingly.

$I_{\text{scatt}}^* = 1$ corresponds to insulating and $I_{\text{scatt}}^* = 0$ to metallic phase. In order to define the point of steepest slope of the hysteresis, dI_{scatt}^*/dT derivatives were calculated. Here, the thermal range between minima of dI_{scatt}^*/dT curves is defined as a characteristic width ΔT of the hysteresis. Thus, Fig. 7(b) shows the same $\Delta T = 3.5$ K for structures with different spatial frequencies. Nevertheless, the hysteresis is different for different structures: it noticeably broadens at higher spatial frequencies. This broadening is assigned to stronger misfit strain and higher concentration of structural defects in smaller grains.^{10,11,63}

Other important aspects which can be monitored by light scattering are fluctuations of density and entropy due to defects, strains, and coexistence of insulator and metallic phases near the critical point.⁶⁴ These factors increase fluctuation of the dielectric constant ϵ as the temperature approaches the PT point and, as a consequence, increase the scattering signal. This appears as a sharp rise of the scattering [dashed portion in Fig. 7(a)], and referenced as “transition opalescence.”⁶⁵ It is remarkable that such a scattering feature is more pronounced and broader for smaller grains. This result proves the heretofore debatable opinion that the smallest VO_2 grains are under relatively high and random local elastic strains from the substrate and neighbouring grains, and can contain larger number of oxygen vacancy defects which provide significant system disorder at the critical point.

Influence of the film thickness on structural transformation of the film

It was found that the increase of the film thickness above some critical value results in noticeable changes of scattering and hysteresis properties. Thus, the integrated scattering intensity for 125-nm-thick PLD film is increased by a factor of two with respect to the 30-nm-thick film, indicating increased surface roughness by a factor of $\sim\sqrt{2}$.³³ The distribution of VO_2 crystallites in the thicker film has a higher degree of isotropy, resulting in almost complete blurring of the rectangular shape of isophotes in Fig. 8(a), particularly at higher spatial frequencies. Nevertheless, this distribution is not random and forms strongly ordered groups of crystallites.

The cross-section of the scattering indicatrix along an arbitrary direction shows equidistant BSDF(f) maxima [Fig. 8(b)]. Thus, separation of BSDF(f) peaks for azimuthal directions $\varphi = 47^\circ$ is $\Delta f = 8.7 \times 10^{-2} \mu\text{m}^{-1}$. The BSDF(f) with equidistant maxima is related to corrugated surface relief and can be modeled by superposition of light scattering from a diffraction grating of several lines superimposed onto a stochastic surface relief. The modeling of BSDF(f) using the equation for the intensity of light diffraction by periodic structures^{66,67}

$$I_{DG} = I_0^D \left(\frac{\sin(N\pi df)}{\sin(\pi df)} \right)^2 \left(\frac{\sin(\pi sf)}{\pi sf} \right)^2, \quad (5)$$

shows good coincidence with experimental data when the diffraction grating consists of $N = 3$ lines with period $d = 12 \mu\text{m}$, separated by boundaries with width $s = 0.61 \mu\text{m}$. Here, I_0^D is maximal diffraction intensity. The location of the

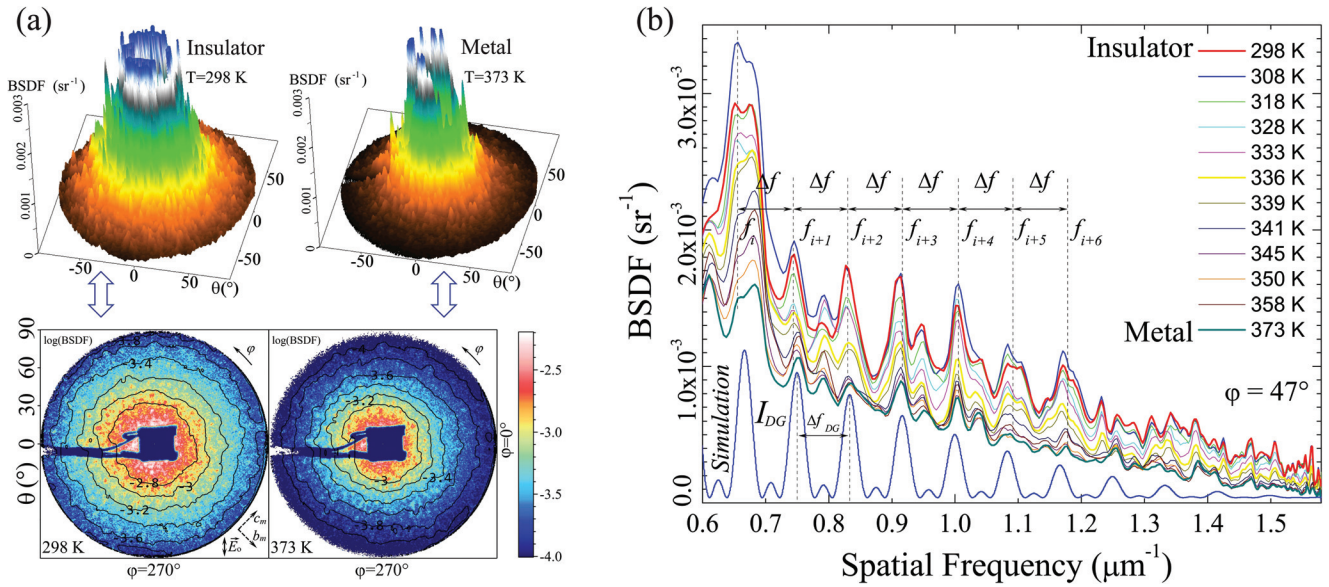


FIG. 8. Light scattering by 125-nm-thick film $\text{VO}_2/\text{Al}_2\text{O}_3$ (r-cut). (a) Scattering indicatrices for insulating and metallic phases. (b) Cross-section of BSGDF indicatrix. I_{DG} is the simulated diffraction intensity for diffraction grating with $N=3$, $d=12\ \mu\text{m}$, and $s=0.61\ \mu\text{m}$. (Multimedia view) [URL: <http://dx.doi.org/10.1063/1.4921057.3>]

equidistant diffraction peaks I_{DG} , their separation $\Delta f_{DG} = 8.3 \times 10^{-2}\ \mu\text{m}^{-1}$, as well as presence and positions of minor diffraction peaks are very close to those in the experimental BSGDF(f) data [Fig. 8(b)]. This model assumes that the VO_2 crystallites organize as relatively large ordered $12\ \mu\text{m}$ domains, separated by a $0.61\ \mu\text{m}$ boundary formed by one or two crystallites. Moreover, since epitaxial VO_2 film can be considered as a “supercrystal,” as discussed above, it is expected that the large $12\ \mu\text{m}$ domains also contain ordered sub-structures with spatial frequencies $f_i = i \times \Delta f_{DG}$, where i is the number of diffraction order.

The theoretical modeling of light diffraction is shown for single periodical structure with $N=3$. However, the real surface of epitaxial film is the ensemble of ordered but different in shape VO_2 grains. This system has noticeable stochastic component that contributes to the scattering indicatrix, resulting in slight difference between positions of some diffraction peaks obtained experimentally and from theoretical calculation [Fig. 8(b)].

Despite similar scattering indicatrices for 30-nm- and 125-nm-thick films $\text{VO}_2/\text{Al}_2\text{O}_3$ (r-cut) [Figs. 1(a) and 8(a)], there is considerable difference in their temperature-dependent structural transformation. The BSGDF(f) of the thinner film shows significant qualitative change at different temperatures (Figs. 1(a) and 4), but the 125-nm-thick film shows almost uniform decay of diffraction peaks *without any significant shift or distortion* [Fig. 8(b)]. When VO_2 is switched into its metallic phase, the local BSGDF(f) maxima are suppressed at $T=373\text{ K}$, but their positions remain the same. This indicates that the domain pattern of the 125-nm-thick film remains also the same, and no additional twinning or “dynamic” temperature-dependent reorganization of domains occurs. It is very likely that the static domain structure is formed during the PLD process via generation of the dislocation network and introduction of new grain boundaries or microcracks.

The VO_2 PLD film on r-cut Al_2O_3 substrate is mismatched, with misfit strain $\epsilon_m = 4.0\%$ along $[010]_{\text{VO}_2}$ and $\epsilon_m = -5.1\%$ along $[001]_{\text{VO}_2}$.⁴¹ If the thickness is smaller than the critical value h_c , the film is maximally strained but free of MDs.^{68,69} However, when the thickness exceeds the threshold h_c , the MD network abruptly appears to reduce the misfit strain. Data obtained for the 125-nm-thick $\text{VO}_2/\text{Al}_2\text{O}_3$ (r-cut) film indicate that the thickness of this film is above h_c . Thus, the PLD at $T=825\text{ K}$ has formed a flat epitaxial film in tetragonal phase with relatively high concentration of MDs. It is also very likely that when the film is cooled down to room temperature after the deposition, different thermal expansion of the film and substrate along with the VO_2 volume contraction by $\sim 0.044\%$ (Ref. 60) resulted in additional generation of dislocations, new grain boundaries, or microcracks with self-organization of VO_2 domains into periodical structures. Once generated, the network of structural defects then significantly contributes to the PT process. These defects prevent a “dynamic” temperature-dependent twinning of 125-nm-thick film during the PT, as compared to the thinner film. As a result, sharp BSGDF(f) peaks in scattering indicatrix do not shift, but decay as temperature increases [Fig. 8(b)].

As shown previously for VO_2/Si samples prepared by RF sputtering,²² the absolute value of residual stress drops by more than nine times, as the film thickness increases from 100 nm to 440 nm. For the epitaxial $\text{VO}_2/\text{Al}_2\text{O}_3$ (r-cut) PLD films, the strain and stress both are noticeably suppressed already for 125-nm-thick film due to introduction of structural defects, as revealed from the evolution of scattering pattern in Fig. 8(b). The alteration of the stress during the PT is small enough and insufficient to produce the film twinning or formation of new domains.

The relative change of the scattering signal allows to identify spatial frequencies of VO_2 domains with different PT properties. Thus, the $\Delta\text{BSDF}(T)/\text{BSDF}_0$ indicatrix in Fig. 9(a)

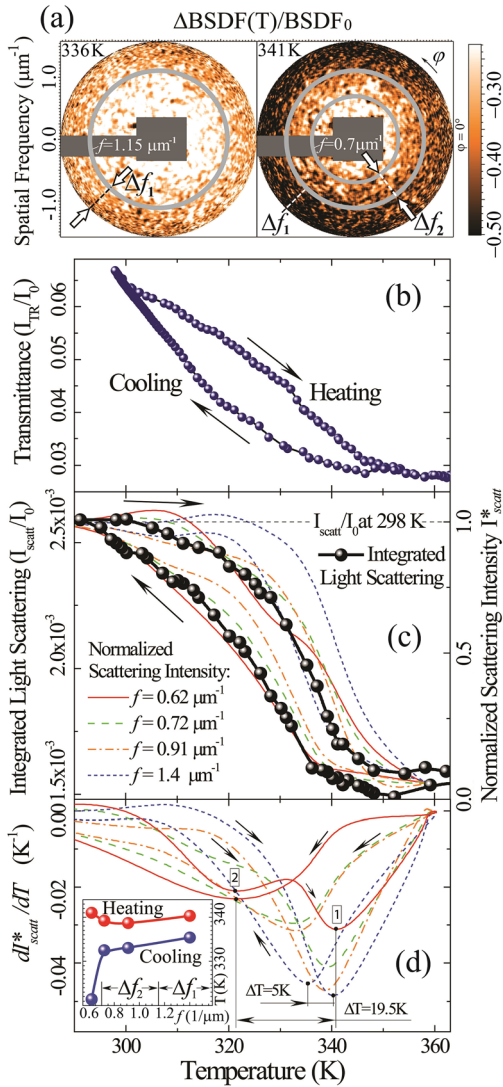


FIG. 9. Optical properties of 125-nm-thick VO₂/Al₂O₃(r-cut) film near the PT point. (a) The relative change of scattering signal at $T=336\text{ K}$ and $T=341\text{ K}$. (b) Hysteretic evolution of transmittance at $\lambda=1310\text{ nm}$. (c) Scattering signal I_{scatt}/I_0 integrated within hemisphere and signal I_{scatt}^* for different spatial frequencies of the surface. (d) Derivative of the hysteresis curves. Inset shows location of dI_{scatt}^*/dT minima versus spatial frequency.

can be divided into three regions: $\Delta f_1 = 1.15\text{--}1.58\ \mu\text{m}^{-1}$ (size range is $0.633\text{--}0.870\ \mu\text{m}$), $\Delta f_2 = 0.7\text{--}1.15\ \mu\text{m}^{-1}$ (size range is $0.870\text{--}1.43\ \mu\text{m}$), and region with $f < 0.7\ \mu\text{m}^{-1}$ ($d > 1.43\ \mu\text{m}$). Near the PT point, at $T=336\text{ K}$, the scattering signal drops uniformly within the region Δf_1 with higher rate. As the temperature approaches $T=341\text{ K}$, the signal continuously decreases, but with noticeably different rate for each region, indicating different PT dynamics for domains of different size.

The VO₂/Al₂O₃ films used in this study are epitaxial and nearly stoichiometric, but their different microstructure significantly affects the thermal hysteresis. The hysteresis loop of optical transmittance and integrated light scattering for the 125-nm-thick film [Figs. 9(b) and 9(c)] is much broader and significantly tilted as compared to the hysteresis of the thinner film [see Fig. 7(a)]. This difference is attributed to the higher concentration of structural defects in the 125-nm-thick film. As was discussed above, the strain field in this

film is significantly reduced due to high density of MDs. Therefore, the broad and tilted hysteresis in Figs. 9(b) and 9(c) has no significant relation to the strain but rather to the presence of defects. The structural defects shift the PT temperature. During the PT, some domain walls are pinned by defects, contributing to the distortion of the hysteresis shape and width.

The hysteresis of optical transmittance I_{TR}/I_0 does not coincide exactly with that of integrated light scattering I_{scatt}/I_0 [Figs. 9(b) and 9(c)], since the scattered light is additionally affected by structural and dielectric constant inhomogeneity. Hysteresis loops I_{scatt}^*/I_0 show significant grain-size-dependence. Using the derivatives dI_{scatt}^*/dT [Fig. 9(d)], the characteristic hysteresis width for $f=0.62\ \mu\text{m}^{-1}$ is found to be $\Delta T=19.5\text{ K}$. However as soon as spatial frequency exceeds $0.7\ \mu\text{m}^{-1}$, the hysteresis width shrinks to $\Delta T=5\text{ K}$ and weakly depends on f . Along with narrowing of hysteresis, the second principal feature of Fig. 9(c) is a gradual shift of the hysteresis loop with its steeper slope to higher f , as the spatial frequency increases. Here, at the higher spatial frequency $f=1.4\ \mu\text{m}^{-1}$, the hysteresis width and position remarkably approaches those values related to thinner film [see Fig. 7(a)], indicating similar physical properties of the 30-nm-thick film and grains of the 125-nm-thick film with $f=1.4\ \mu\text{m}^{-1}$.

The observed behavior of hysteresis loops for different spatial frequencies evidences a gradual size-dependent change of structural parameters. The MD network is assumed as the main origin which affects the thermal hysteresis. The broad hysteresis $\Delta T=19.5\text{ K}$ for $f < 0.7\ \mu\text{m}^{-1}$ and its abrupt change to $\Delta T \approx 5\text{ K}$ above $f=0.7\ \mu\text{m}^{-1}$ [see Fig. 9(d), inset] indicates that the larger structures with $f < 0.7\ \mu\text{m}^{-1}$ contain higher densities of MDs. The pinning of domain walls by defects changes the tilt of the hysteresis loop and possibly is the origin of the second minimum [2] in the dI_{scatt}^*/dT curve for $f=0.62\ \mu\text{m}^{-1}$. The significant change of the hysteresis width and slope at $f=0.7\ \mu\text{m}^{-1}$ indicates a possible presence of a “transverse” threshold for the generation of MDs at this spatial frequency. Above $f=0.7\ \mu\text{m}^{-1}$ the concentration of MDs rapidly drops and continuously decreases for smaller grains. Thus, already at $f=1.4\ \mu\text{m}^{-1}$, the hysteresis loop of the 125-nm-thick film approaches in shape that of the 30-nm-thick film, which is almost free of MDs.

CONCLUSION

In this paper, the influence of strain and structural defects on thermally induced PT of epitaxial VO₂/Al₂O₃ films has been discussed. The angle-resolved light scattering measurements show that the elastic strain significantly affects the thermal transition, resulting in temperature-dependent twinning of microcrystallites and domain formation at temperatures much below the PT point T_c . The scattering indicatrix, surface power spectral density, and autocorrelation function demonstrate distinctive qualitative change during the transition. At the critical temperature T_c , disorder of the 30-nm-thick film reaches the highest level due to coexistence of insulating and metallic phases. Here, the surface autocorrelation length drops to its minimal value. However, when

VO₂ switches into metallic state, the autocorrelation length recovers back, close to its initial value in the insulating phase. As the film switches from M₁ to R-phase, the fractal dimension of the surface decreases, indicating smother surface with more uniform optical properties in the metallic phase. It is shown that the hysteresis loop depends on spatial frequency of surface irregularities. Smaller grains of 30-nm-thick film have broader hysteresis and noticeable “transition opalescence” due to higher elastic strain and higher concentrations of point defects.

When the film thickness exceeds the threshold value for the introduction of misfit dislocations, these dislocations noticeably suppress the internal strain in the film. Thus, the strain in relatively thick 125-nm film is substantially reduced, showing considerably different light scattering and structural evolution upon thermally induced PT, as compared to the strained 30-nm-thick film with lower concentration of misfit dislocations. The broadening of the hysteresis loop increases with concentration of dislocations, since domain walls of a new phase are pinned by defects. In the absence of internal strain, the BSDF scattering pattern does not change qualitatively with temperature, indicating the absence of temperature-dependent film twinning or formation of new domain pattern.

The considerably different evolution of the scattering indicatrix for the films with higher internal elastic strain and for thicker films where this strain is suppressed by misfit dislocations opens new possibilities for selection and classification of these films by angle-resolved light scattering technique.

ACKNOWLEDGMENTS

The authors gratefully acknowledge the support from UPRM College of Arts and Sciences. N.S. was supported in part by the National Science Foundation under Grant No. ECCS-1139773.

- ¹F. J. Morin, *Phys. Rev. Lett.* **3**, 34 (1959).
- ²Z. Yang, C. Ko, and S. Ramanathan, *Annu. Rev. Mater. Res.* **41**, 337 (2011).
- ³J. D. Ryckman, K. A. Hallman, R. E. Marvel, R. F. Haglund, and S. M. Weiss, *Opt. Express* **21**, 10753 (2013).
- ⁴M. J. Dicken, K. Aydin, I. M. Pryce, L. A. Sweatlock, E. M. Boyd, S. Walavalkar, J. Ma, and H. A. Atwater, *Opt. Express* **17**, 18330 (2009).
- ⁵H. Coy, R. Cabrera, N. Sepúlveda, and F. E. Fernández, *J. Appl. Phys.* **108**, 113115 (2010).
- ⁶M. A. Kats, R. Blanchard, P. Genevet, Z. Yang, M. M. Qazilbash, D. N. Basov, S. Ramanathan, and F. Capasso, *Opt. Lett.* **38**, 368 (2013).
- ⁷M. M. Qazilbash, Z. Q. Li, V. Podzorov, M. Brehm, F. Keilmann, B. G. Chae, H. T. Kim, and D. N. Basov, *Appl. Phys. Lett.* **92**, 241906 (2008).
- ⁸M. Maaza, A. Simo, B. Itani, J. Kana Kana, S. El Harthi, K. Bouziane, M. Saboungi, T. Doyle, and I. Luk'yanchuk, *J. Nanopart. Res.* **16**, 2397 (2014).
- ⁹I. A. Khakhaev, F. A. Chudnovskii, and E. B. Shadrin, *Phys. Solid State* **36**, 898 (1994).
- ¹⁰R. Aliev, V. Andreev, V. Kapralova, V. Klimov, A. Sobolev, and E. Shadrin, *Phys. Solid State* **48**, 929 (2006).
- ¹¹V. Klimov, I. Timofeeva, S. Khanin, E. Shadrin, A. Ilinskii, and F. Silva-Andrade, *Tech. Phys.* **47**, 1134 (2002).
- ¹²R. Lopez, T. E. Haynes, L. A. Boatner, L. C. Feldman, and R. F. Haglund, *Phys. Rev. B* **65**, 224113 (2002).
- ¹³R. Lopez, L. C. Feldman, and R. F. Haglund, *Phys. Rev. Lett.* **93**, 177403 (2004).
- ¹⁴M. C. Newton, M. Sao, Y. Fujisawa, R. Onitsuka, T. Kawaguchi, K. Tokuda, T. Sato, T. Togashi, M. Yabashi, T. Ishikawa, T. Ichitsubo, E. Matsubara, Y. Tanaka, and Y. Nishino, *Nano Lett.* **14**, 2413 (2014).
- ¹⁵K. Liu, C. Cheng, J. Suh, R. Tang-Kong, D. Fu, S. Lee, J. Zhou, L. O. Chua, and J. Wu, *Adv. Mater.* **26**, 1746 (2014).
- ¹⁶A. Tselev, E. Strelcov, I. A. Luk'yanchuk, J. D. Budai, J. Z. Tischler, I. N. Ivanov, K. Jones, R. Proksch, S. V. Kalinin, and A. Kolmakov, *Nano Lett.* **10**, 2003 (2010).
- ¹⁷M. S. Grinolds, V. A. Lobastov, J. Weissenrieder, and A. H. Zewail, *PNAS* **103**, 18427 (2006).
- ¹⁸A. Frenzel, M. M. Qazilbash, M. Brehm, B.-G. Chae, B.-J. Kim, H.-T. Kim, A. V. Balatsky, F. Keilmann, and D. N. Basov, *Phys. Rev. B* **80**, 115115 (2009).
- ¹⁹M. M. Qazilbash, M. Brehm, B.-G. Chae, P.-C. Ho, G. O. Andreev, B.-J. Kim, S. J. Yun, A. V. Balatsky, M. B. Maple, F. Keilmann, H.-T. Kim, and D. N. Basov, *Science* **318**, 1750 (2007).
- ²⁰M. M. Qazilbash, A. Tripathi, A. A. Schafgans, B.-J. Kim, H.-T. Kim, Z. Cai, M. V. Holt, J. M. Maser, F. Keilmann, O. G. Shpyrko, and D. N. Basov, *Phys. Rev. B* **83**, 165108 (2011).
- ²¹A. Tselev, V. Meunier, E. Strelcov, W. A. Shelton, I. A. Luk'yanchuk, K. Jones, R. Proksch, A. Kolmakov, and S. V. Kalinin, *ACS Nano* **4**, 4412 (2010).
- ²²V. Balakrishnan, C. Ko, and S. Ramanathan, *J. Mater. Res.* **26**, 1384 (2011).
- ²³J. Sakai, M. Zaghrioui, M. Matsushima, H. Funakubo, and K. Okimura, *J. Appl. Phys.* **116**, 123510 (2014).
- ²⁴C. Chen, Y. Zhao, X. Pan, V. Kuryatkov, A. Bernussi, M. Holtz, and Z. Fan, *J. Appl. Phys.* **110**, 023707 (2011).
- ²⁵S. Lysenko, F. Fernandez, A. Rua, and H. Liu, *J. Appl. Phys.* **114**, 153514 (2013).
- ²⁶S. Lysenko, F. Fernandez, A. Rua, N. Sepulveda, and J. Aparicio, *Appl. Opt.* **54**, 2141 (2015).
- ²⁷M. Zerrad, M. Lequime, and C. Amra, *Appl. Opt.* **53**, A297 (2014).
- ²⁸J. Sorrentini, M. Zerrad, and C. Amra, *Opt. Lett.* **34**, 2429 (2009).
- ²⁹V. Sterligov, Y. Subbota, Y. Shirshov, L. Pochekeylova, E. Venger, R. Konakova, and I. Ilyin, *Appl. Opt.* **38**, 2666 (1999).
- ³⁰S. Schröder, A. Duparré, L. Coriand, A. Tünnermann, D. H. Penalver, and J. E. Harvey, *Opt. Express* **19**, 9820 (2011).
- ³¹J. E. Harvey, S. Schröder, N. Choi, and A. Duparré, *Opt. Eng.* **51**, 013402 (2012).
- ³²T. Herfurth, S. Schröder, M. Trost, A. Duparré, and A. Tünnermann, *Appl. Opt.* **52**, 3279 (2013).
- ³³J. C. Stover, *Optical Scattering: Measurements and Analysis* (SPIE Optical Engineering Press, Bellingham, Washington, 1995).
- ³⁴J. M. Elson, *Waves Random Media* **7**, 303 (1997).
- ³⁵I. Horcas, R. Fernández, J. M. Gómez-Rodríguez, J. Colchero, J. Gómez-Herrero, and A. M. Baro, *Rev. Sci. Instrum.* **78**, 013705 (2007).
- ³⁶A. L. Roitburd, *Solid State Phys.* **33**, 317 (1978).
- ³⁷J. Budai, A. Tselev, J. Tischler, E. Strelcov, A. Kolmakov, W. Liu, A. Gupta, and J. Narayan, *Acta Mater.* **61**, 2751 (2013).
- ³⁸A. Tselev, I. A. Luk'yanchuk, I. N. Ivanov, J. D. Budai, J. Z. Tischler, E. Strelcov, A. Kolmakov, and S. V. Kalinin, *Nano Lett.* **10**, 4409 (2010).
- ³⁹J. Cao, E. Ertekin, V. Srinivasan, W. Fan, S. Huang, H. Zheng, J. W. L. Yim, D. R. Khanal, D. F. Ogletree, J. C. Grossman, and J. Wu, *Nat. Nanotechnol.* **4**, 732 (2009).
- ⁴⁰M. Liu, M. Wagner, J. Zhang, A. McLeod, S. Kittiwatanakul, Z. Fei, E. Abreu, M. Goldflam, A. J. Sternbach, S. Dai, K. G. West, J. Lu, S. A. Wolf, R. D. Averitt, and D. N. Basov, *Appl. Phys. Lett.* **104**, 121905 (2014).
- ⁴¹T.-H. Yang, R. Aggarwal, A. Gupta, H. Zhou, R. J. Narayan, and J. Narayan, *J. Appl. Phys.* **107**, 053514 (2010).
- ⁴²S. Lysenko, V. Vikhnin, F. Fernandez, A. Rua, and H. Liu, *Phys. Rev. B* **75**, 075109 (2007).
- ⁴³Y. Zhao, J. Hwan Lee, Y. Zhu, M. Nazari, C. Chen, H. Wang, A. Bernussi, M. Holtz, and Z. Fan, *J. Appl. Phys.* **111**, 053533 (2012).
- ⁴⁴Z. P. Wu, S. Yamamoto, A. Miyashita, Z. J. Zhang, K. Narumi, and H. Naramoto, *J. Phys.: Condens. Matter* **10**, L765 (1998).
- ⁴⁵M. Borek, F. Qian, V. Nagabushnam, and R. K. Singh, *Appl. Phys. Lett.* **63**, 3288 (1993).
- ⁴⁶D. Fu, K. Liu, T. Tao, K. Lo, C. Cheng, B. Liu, R. Zhang, H. A. Bechtel, and J. Wu, *J. Appl. Phys.* **113**, 043707 (2013).
- ⁴⁷X. Li, A. Gloter, H. Gu, X. Cao, P. Jin, and C. Colliex, *Acta Mater.* **61**, 6443 (2013).
- ⁴⁸J. I. Sohn, H. J. Joo, A. E. Porter, C.-J. Choi, K. Kim, D. J. Kang, and M. E. Welland, *Nano Lett.* **7**, 1570 (2007).

- ⁴⁹M. H. Kim, B. Lee, S. Lee, C. Larson, J. M. Baik, C. T. Yavuz, S. Seifert, S. Vajda, R. E. Winans, M. Moskovits, G. D. Stucky, and A. M. Wodtke, *Nano Lett.* **9**, 4138 (2009).
- ⁵⁰A. L. Roytburd, J. Ouyang, B. M. Boyerinas, and H. A. Bruck, *Appl. Phys. Lett.* **99**, 172902 (2011).
- ⁵¹E. L. Church, *Appl. Opt.* **27**, 1518 (1988).
- ⁵²M. V. Berry, *J. Phys. A* **12**, 781 (1979).
- ⁵³M. V. Berry and Z. V. Lewis, *Proc. R. Soc. London, Ser. A* **370**, 459 (1980).
- ⁵⁴T. G. Lanskaya, I. A. Merkulov, and F. A. Chudnovskii, *Sov. Phys. Solid State* **20**, 193 (1978).
- ⁵⁵R. W. Gerchberg and W. O. Saxton, *Optik* **35**, 237 (1972).
- ⁵⁶J. R. Fienup, *Appl. Opt.* **21**, 2758 (1982).
- ⁵⁷J. M. Atkin, S. Berweger, E. K. Chavez, M. B. Raschke, J. Cao, W. Fan, and J. Wu, *Phys. Rev. B* **85**, 020101 (2012).
- ⁵⁸J. I. Sohn, H. J. Joo, K. S. Kim, H. W. Yang, A.-R. Jang, D. Ahn, H. HwiLee, S. Cha, D. J. Kang, J. M. Kim, and M. E. Welland, *Nanotechnology* **23**, 205707 (2012).
- ⁵⁹S. Zhang, J. Y. Chou, and L. J. Lauhon, *Nano Lett.* **9**, 4527 (2009).
- ⁶⁰D. Kucharczyk and T. Niklewski, *J. Appl. Crystallogr.* **12**, 370 (1979).
- ⁶¹K. V. K. Rao, S. V. N. Naidu, and L. Iyengar, *J. Am. Ceram. Soc.* **53**, 124 (1970).
- ⁶²A. Roitburd, *JETP Lett.* **15**, 300 (1972); available at http://www.jetpletters.ac.ru/ps/1750/article_26611.shtml.
- ⁶³Z. Hiroi and Y. Muraoka, *Appl. Phys. Lett.* **80**, 583 (2002).
- ⁶⁴V. L. Ginzburg, A. P. Levanyuk, and A. A. Sobyenin, *Phys. Rep.* **57**, 151 (1980).
- ⁶⁵K. A. Valiev, V. G. Mokerov, V. V. Sarajkin, and A. G. Petrova, *Sov. Phys. Solid State* **19**, 1487 (1977).
- ⁶⁶M. Born, E. Wolf, and A. Bhatia, *Principles of Optics: Electromagnetic Theory of Propagation, Interference and Diffraction of Light* (Cambridge University Press, 1999).
- ⁶⁷V. Sterligov, Y. Men, and P. Lytvyn, *Opt. Express* **18**, 43 (2010).
- ⁶⁸J. Y. Tsao, *Materials Fundamentals of Molecular Beam Epitaxy* (Academic Press, London, 1992).
- ⁶⁹J. S. Speck and W. Pompe, *J. Appl. Phys.* **76**, 466 (1994).